

# Nanoscale heat transfer investigation of an array of impinging jet systems with different working fluids under crossflow with and without pin fins

Usman Allaardin<sup>1</sup>  | Rafay Mohiuddin<sup>1</sup> |  
Hafiz Mohammad Usman Khan<sup>1</sup> | Naseem Uddin<sup>2</sup> |  
Waqar A. Khan<sup>3</sup>

<sup>1</sup>Department of Mechanical Engineering,  
NED University of Engineering and  
Technology, Karachi, Pakistan

<sup>2</sup>Mechanical Engineering Program,  
Universiti Teknologi Brunei, Gadong,  
Brunei

<sup>3</sup>Department of Mechanical Engineering,  
Prince Mohammad Bin Fahd University,  
Al Khobar, Saudi Arabia

## Correspondence

Usman Allaardin, Department of  
Mechanical Engineering, NED University  
of Engineering and Technology,  
Karachi 75270, Pakistan.

Email: [usman.allaardin@neduet.edu.pk](mailto:usman.allaardin@neduet.edu.pk)

## Funding information

The Higher Education Commission (HEC),  
Pakistan, Grant/Award Number:  
SRGP 2067

## Abstract

In the current numerical study, the thermal and flow field performance of an array of confined multiple jets with air, water, and water-Al<sub>2</sub>O<sub>3</sub> nanofluid in the maximum crossflow configuration over the target plate with and without pin fins is investigated. The numerical results are validated with the experimental data; it is found that a reasonable prediction related to heat transfer can be made. For this study, steady-state Reynolds-averaged Navier-Stokes simulations with the shear-stress transport  $k-\omega$  turbulence model in ANSYS Fluent were performed. The simulations are performed with volumetric concentration  $\phi = 0.2\%$  to  $3\%$  and the jet's Reynolds number  $Re = 15\,000$  to  $35\,000$ . In all cases, the jet outlet-to-target plate distance  $Z/D$  is 3. It is found that the increase in values of the volumetric concentration of nanoparticles results in a decrease of the Nusselt number and an increase of the convective heat transfer coefficient. This is because there is an increase in thermal conductivity of the working fluid with the increase in the volumetric concentration of nanoparticles for the same Reynolds number. About 81.5% and 89.1%

enhancement in the average heat transfer flux values is observed for flat and pin fin-roughened target plates, respectively, for  $\phi = 3\%$ .

#### KEY WORDS

computational fluid dynamics, heat transfer enhancement, impinging jet, multiple jets, nanofluid, pin fins, water-Al<sub>2</sub>O<sub>3</sub>

## 1 | INTRODUCTION

The large-scale industrial applications involving high heat transfer rates, for example, cooling of gas turbine components, heats sinks, electronics components, and so in, often utilize jet impingement systems. To improve the efficiency of a high-performance thermal system, it is important to enhance heat transfer rates. The multiple jet impingement systems are more complex than the single jet impingement systems due to the interaction of different flow parameters. Zuckerman and Lior<sup>1</sup> discussed various parameters affecting the performance of impinging jet systems. Different empirical correlations and numerical techniques were also reviewed by the authors. Martin<sup>2</sup> and Weigand and Spring<sup>3</sup> reviewed flow physics and different parameters affecting the heat transfer augmentation, which provides a good understanding related to multiple jet impingement.

The thermal performance of impinging jets systems can be increased by enhancing the surface area of the target plate by adding fins, ribs, dimples, and so on. In the past, various studies were performed to examine a range of configurations of impinging jet systems. Xing et al<sup>4</sup> performed a comparison of the thermal characteristics of air-jet impingement on staggered and inline configurations of pin fins over the target plate. They conducted the study for different crossflow schemes, jet outlet-to-target wall spacing  $Z/D$  ranging from 3 to 5, and  $Re = 15\,000, 25\,000$ , and  $35\,000$ . They found that a high crossflow, high  $Re$ , and low  $Z/D$  values yield the best heat transfer characteristics. The inline configuration produced better heat transfer rates as compared with the staggered one. Wae-Hayee et al<sup>5</sup> compared staggered and inline nozzle arrangements of 24 impinging jet arrays with  $Z/D = 2$  for Reynolds numbers 5000, 7000, and 13 400. The Nusselt numbers for the inline configuration were found to be 13% to 20% higher than the Nusselt numbers observed in the staggered configuration. Caliskan et al<sup>6</sup> studied the flow and heat transfer characteristics for multiple jets having elliptical and rectangular nozzle geometries with different aspect ratios at Reynolds number = 2000 to 10 000 and  $Z/D = 1$  to 10. They found that geometries with a higher aspect ratio yield better results, whereas the elliptical jets resulted in a higher thermal performance than the rectangular jets. About 6.0% to 16.8% enhancement in the thermal performance was reported in their study. Spring et al<sup>7</sup> studied the ribs effect in an array of impinging jet systems with the maximum crossflow at  $Re = 35\,000$  and  $Z/D = 3$ . In the first configuration, ribs were placed perpendicular to the crossflow, whereas in the second one, the ribs were in a staggered arrangement, parallel to the crossflow. The latter configuration yielded better heat transfer results. It was concluded that the effect of the area should be considered when comparing the amount of transferred heat flux. Xing et al<sup>8</sup> studied the thermal performance of the plate roughened with microribs for  $Z/D = 3$  to 5 and  $Re = 15\,000$  to  $35\,000$ . About 9.6% augmentation in the thermal performance, compared with the flat plate, was observed. Rao et al<sup>9</sup> determined heat transfer characteristics of the target

plate roughened with W-shaped microribs for the case of multiple impinging jets under the maximum crossflow configuration. They found a considerable enhancement in the thermal performance as compared with the flat plate for  $Re = 3000$  with a negligible pressure drop. Chen et al<sup>10</sup> studied different configurations of V-ribs mounted on the target and impingement plates. The formation of secondary flow structures, due to the presence of V-ribs, resulted in positive heat flux ratios of 1.06 to 1.34. Wan et al<sup>11</sup> studied the thermal performance of multiple jets with and without surface enlargement elements. The inline pin fins configuration yielded better results. An overall increment in heat transfer, up to 34.5%, and a decrement in the discharge coefficient, of 3.0%, were observed.

The heat transfer rates of jet impingement systems can also be increased by the usage of nanoparticles in the base fluid. Nanoparticles have high thermophysical characteristics that augment the thermal performance of jet impingement systems. The effects of nanoparticles on the heat transfer performance of impinging jets are investigated in many experimental studies. Zeitoun and Ali<sup>12</sup> conducted experiments to determine the thermal performance of  $\text{Al}_2\text{O}_3$  nanoparticles in water-jet impingement over a flat plate with  $\phi = 0\%$ , 6.6%, and 10%. They found that at a constant  $Re$ , the increasing values of  $\phi$  result in the enhancement of thermal performance, whereas an increase in the size of the disc would result in an opposite effect. Furthermore, an increment in the concentration of nanoparticles increases the absolute viscosity, causing a reduction in the Reynolds number. Modak et al<sup>13</sup> also investigated the thermal performance of  $\text{Al}_2\text{O}_3$  nanoparticles in water-jet impingement over a vertical plate for different  $\phi$  values of  $\text{Al}_2\text{O}_3$  nanoparticles (0.15% and 0.6%), Reynolds number (5000-12 000), and jet-to-target plate distance ( $Z/D = 6$  and 12). They found 112.8% and 32.6% increase in surface heat flux for 0.15% and 0.6% volumetric concentration, respectively. Modak et al<sup>14</sup> also performed another study with a similar setup and found a considerable enhancement in the thermal performance by using  $\text{CuO}$  nanoparticles. Naphon et al<sup>15</sup> conducted experiments to investigate the thermal performance of a jet impingement system in a mini-rectangular pin fin heat sink with different plate widths and mass flow rates. They found a reduction in CPU's temperature with the jet impingement configuration. Barewar et al,<sup>16</sup> used a water-ZnO nanofluid in an impinging jet over a heated copper plate to investigate its heat transfer characteristics. They conducted the experiments with different concentrations of nanoparticles (0.02%-0.1%),  $Z/D$  ratios (2-7.5), and Reynolds numbers (2192-9241). About 51% improvement in the thermal performance for 0.1% volumetric concentration at  $Z/D = 3.5$  was observed. Londhe et al<sup>17</sup> studied the thermal and pumping performance of the ethylene glycol- $\text{Al}_2\text{O}_3$  nanofluid. They conducted experiments for different volumetric concentrations (0%, 0.2%, 0.25%, and 0.3%) of nanoparticles. They observed an improvement in the thermal performance with increasing  $\phi$  values. Compared with the base fluid, about 24%, 33%, and 44% increment in heat transfer coefficient was observed at the volumetric concentrations of 0.2%, 0.25%, and 0.3%, respectively. Nguyen et al<sup>18</sup> performed an experimental investigation using an  $\text{Al}_2\text{O}_3$ -water nanofluid for single, confined, and submerged impinging jets for different Reynolds numbers (3800-88 000), Prandtl numbers (5-10), and volumetric concentrations (0%-6%).

Various numerical studies dealing with the nanofluid jet impingement systems were also conducted by different researchers. Recently, Allauddin et al<sup>19</sup> in their numerical study found a satisfactory agreement of the numerically predicted results with the experimental data of the study reported in Reference [12]. ANSYS CFX with the shear-stress transport (SST)  $k-\omega$  turbulence model was used to perform the numerical simulations. They found that the local Nusselt number values normalized with  $Re^{2/3}$  fall on a single curve for  $Z/D$  values used in the

study. Lorenzo et al<sup>20</sup> investigated laminar slot jet impingement in a confined configuration, with a water-Al<sub>2</sub>O<sub>3</sub> nanofluid. They found that the induction of nanoparticles increases the effective thermal conductivity of the nanofluid, which increases the bulk temperature of the nanofluid. The 5% volumetric concentration of Al<sub>2</sub>O<sub>3</sub> results in about 32% increase in the thermal performance and about 3.9 times increment in the pumping power. They also reported that the confinement configuration, *Re*, and volumetric concentrations of nanoparticles affect the vortex intensity. Manca et al<sup>21</sup> studied a slot jet impingement over a constant temperature target wall with Al<sub>2</sub>O<sub>3</sub> nanoparticles. They used a single-phase modeling assumption. The study was conducted for different volumetric concentrations (0%, 1%, 4%, and 6%), normalized jet outlet-to-the target wall distances (4, 6, 8, and 10), and Reynolds numbers (5000-20 000). The nanoparticles produced an increase in the overall thermal conductivity of the working fluid, which increases the bulk temperature. An increase in volumetric concentration also increases the pumping power. Senkal and Torii<sup>22</sup> conducted a combined experimental and numerical study using Al<sub>2</sub>O<sub>3</sub>-water nanofluid multiple free jets for different Reynolds numbers (1000-6000), volumetric concentrations (0.5%, 2%, and 4.9%) and jet spacings (*S/D* = 3, 5, and 7). A reduction in the Nusselt number is reported with an increase in the volumetric concentration.

The nanofluid multiple jet impingement over a roughened target plate under crossflow conditions is a unique but complex configuration. The effects of different nanoparticles are investigated in majority of the studies using relatively simple impinging jet configurations. Darwish et al<sup>23</sup> conducted a review of impinging jet heat transfer studies. It was reported that the open literature lacks the studies investigating the effects of nanoparticles in arrays of jet impingement over the roughened target plates under a crossflow configuration. In the present numerical study, this unique combination is studied. The thermal and fluid flow characteristics of an array of impinging jets with air, water, and water-Al<sub>2</sub>O<sub>3</sub> nanofluid in the maximum crossflow configuration over different surfaces, including flat target plate with and without pin fins, are investigated. The numerical results are validated with the experimental data of Xing et al<sup>4</sup> and Wan et al.<sup>11</sup> Thus, the main objective of the current work is to study the heat transfer and fluid flow characteristics of an array of water-Al<sub>2</sub>O<sub>3</sub> nanofluid impinging jets with and without pin fins under crossflow conditions. Different cases, numerically investigated in the current study, are tabulated in Table 1.

**TABLE 1** Summary of the cases studied in the current work

Case A	Reynolds number: 15 000, 25 000, 35 000 Medium: Air, water, water-Al <sub>2</sub> O <sub>3</sub> Nanofluid with concentration: 0.2%, 0.7%, 1.5%, 3%
Case B	Reynolds number: 15 000, 25 000, 35 000 Medium: Air, water, water-Al <sub>2</sub> O <sub>3</sub> Nanofluid with concentration: 0.2%, 0.7%, 1.5%, 3%

## 2 | GOVERNING EQUATIONS

The continuity, momentum, and energy equations are solved as follows:

Continuity:

$$\frac{\partial U_i}{\partial x_i} = 0. \quad (1)$$

Momentum:

$$\frac{\partial(\rho U_j U_i)}{\partial x_j} = -\frac{\partial P}{\partial x_i} + \frac{\partial}{\partial x_j} \left[ \mu \left( \frac{\partial U_i}{\partial x_j} + \frac{\partial U_j}{\partial x_i} \right) - \rho U_i' U_j' \right]. \quad (2)$$

Energy:

$$\frac{\partial(\rho U_i T)}{\partial x_i} = \frac{\partial}{\partial x_i} \left[ k \frac{\partial T}{\partial x_i} - \rho C_p U_i' T' \right], \quad (3)$$

where  $T$ ,  $P$ , and  $U_i$  represent mean temperature, pressure, and velocity component, respectively, in the  $x_i$  direction, and  $\rho$ ,  $\mu$ , and  $\mu_t$  are the fluid density, dynamic viscosity, and turbulent dynamic viscosity, respectively.  $U_i'$  and  $T'$  represent the fluctuating component of  $U_i$  and  $T$ , respectively. On the basis of Menter's<sup>24</sup> work, the turbulent stresses of momentum and energy equations are modeled by the SST  $k-\omega$  model with viscous subheating and low Reynolds number correction. Turbulence is a transient phenomenon. To accurately model a turbulent impinging jet system, a transient analysis should be done. However, this approach will highly increase the computational cost; hence, a steady-state analysis is done to reduce the computational cost. A similar approach is also used by Brakmann et al<sup>25</sup> and many other researchers.<sup>4,11,19</sup> Zu et al<sup>26</sup> reported that the SST  $k-\omega$  model gives a good computational performance with a comparatively low computational cost for the case of an impinging jet system. Peng et al<sup>27</sup> and Allauddin et al<sup>19</sup> found the SST  $k-\omega$  model to be the most appropriate model for the prediction of heat transfer performance of the nanofluid impinging jet system. Therefore, all numerical simulations reported in the current study are performed with the SST  $k-\omega$  turbulence model:

$$\frac{\partial k}{\partial t} + U_j \frac{\partial k}{\partial x_j} = P_k - \beta * k \omega + \frac{\partial}{\partial x_j} \left[ (\nu - \sigma_k \nu_t) \frac{\partial k}{\partial x_j} \right], \quad (4)$$

$$\frac{\partial \omega}{\partial t} + U_j \frac{\partial \omega}{\partial x_j} = \alpha s^2 - \beta \omega^2 + \frac{\partial}{\partial x_j} \left[ (\nu + \sigma_\omega \nu_t) \frac{\partial \omega}{\partial x_i} \right] + 2(1-F)\sigma_{\omega 2} \frac{1}{\omega} \frac{\partial k}{\partial x_i} \frac{\partial \omega}{\partial x_i}. \quad (5)$$

Eddy viscosity:

$$\nu_t = \frac{\alpha_1 k}{\max(\alpha, \omega, SF_2)}. \quad (6)$$

Closure coefficients and auxiliary relations:

$$F_2 = \tanh \left\{ \left[ \max \left( \frac{2\sqrt{k}}{\beta^* \omega y}, \frac{500U}{y^2 \omega} \right) \right]^2 \right\}, \quad (7)$$

$$P_k = \min \left( \tau_{ij} \frac{\partial v_i}{\partial x_j}, 10\beta^* k \omega \right), \quad (8)$$

$$F_1 = \tanh \left\{ \left\{ \min \left[ \max \left( \left( \frac{2\sqrt{k}}{\beta^* \omega y}, \frac{500U}{y^2 \omega} \right) \right) \frac{4\sigma_{\omega^2} k}{CD_{k\omega} y^2} \right]^4 \right\} \right\}, \quad (9)$$

$$CD_{k\omega} = \max \left( 2\rho\sigma_{\omega^2} \frac{1}{\omega} \frac{\partial k}{\partial x_i} \frac{\partial \omega}{\partial x_i}, 10^{-10} \right), \quad (10)$$

$$\phi = \phi_1 F_1 + \phi_2 (1 - F_1), \quad (11)$$

where  $\alpha_1 = 5/9$ ,  $\alpha_2 = 0.44$ ,  $\beta_1 = 0.075$ ,  $\beta_2 = 0.0828$ ,  $\beta^* = 0.09$ ,  $\alpha_{k1} = 0.85$ ,  $\alpha_{k2} = 1$ ,  $\alpha_{\omega 1} = 1.0$ ,  $\alpha_{\omega 2} = 1/0.586$ .

### 3 | THERMOPHYSICAL PROPERTIES OF THE NANOFUID

A nanofuid is a mixture of highly conductive nanoparticles with a base fluid having relatively low thermal conductivity. Water-Al<sub>2</sub>O<sub>3</sub> is used as a working fluid with constant thermophysical properties in the current study. It is modeled as a single-phase, Newtonian, and incompressible fluid, where the effect of size and shape of nanoparticles is not taken into account. According to Sahoo et al.<sup>28</sup> water-Al<sub>2</sub>O<sub>3</sub> behaves as a Newtonian fluid for 0°C to 90°C and volumetric concentration less than 10%. The thermophysical properties of Al<sub>2</sub>O<sub>3</sub> nanoparticles are taken from the work of Saini and Agarwal,<sup>29</sup> and properties of the base fluid (water) are determined at inlet temperature, as shown in Table 2.

The equivalent thermal conductivity of the nanofuid is determined using the correlation developed by Bhattacharya et al.<sup>30</sup>

$$\lambda_{nf} = (1 - \phi)\lambda_f + \lambda_n, \quad (12)$$

where the nanofuid, base fluid, and nanoparticles are denoted by subscripts nf, f, and n, respectively. For the equivalent viscosity, the correlation by Brinkman<sup>31</sup> is used.

**TABLE 2** Thermophysical properties of water and Al<sub>2</sub>O<sub>3</sub>

Properties	Water	Al <sub>2</sub> O <sub>3</sub>
$\rho$ , kg/m <sup>3</sup>	996.24	4000
$\lambda$ , W/m·K	0.6158	30
$\mu$ , Pa·s	0.0008206	...
$C_p$ , J/kg·K	4179	880

This correlation is a modification of Einstein's equation and can be used for the evaluation of viscosity up to 4% volumetric concentration of nanoparticles:

$$\mu_{\text{nf}} = \frac{\mu_f}{(1 - \phi)^{2.5}}. \quad (13)$$

The equivalent density and specific heat are calculated by the correlations developed by Pak and Cho<sup>32</sup>

$$\rho_{\text{nf}} = (1 - \phi)\rho_f + \rho_n, \quad (14)$$

$$C_{p,\text{nf}} = (1 - \phi)C_{p,f} + C_{p,n}. \quad (15)$$

The properties evaluated using these correlations are tabulated in Table 3.

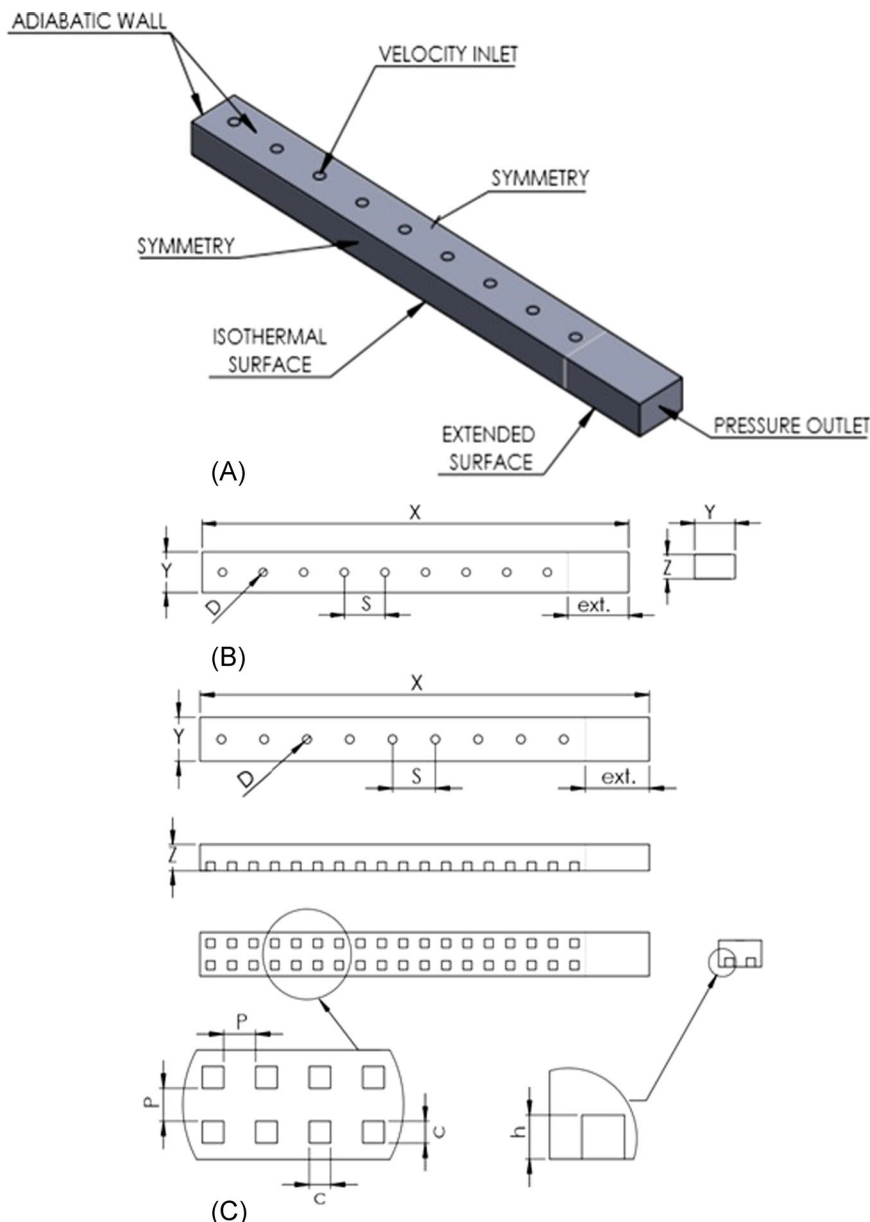
## 4 | COMPUTATIONAL DOMAIN AND BOUNDARY CONDITIONS

Figure 1A shows the computational domain along with the boundary conditions for case A and case B. In the experimental setup, jets were also present perpendicular to the streamwise direction. This is simplified by only considering a row of jets with symmetric boundary conditions. This is shown in Figure 1. The influence of the reverse flow from the outlet is reduced by further extending the outlet of the duct from the last row of fins. The section opposite to the outlet is considered as a wall. It creates confinement and maximum crossflow by directing the flow in one direction. Figures 1B,C show a detailed description of the geometric parameters for case A and case B, respectively. The values of the geometric parameters are tabulated in Tables 4 and 5 for case A and case B, respectively.

The boundary conditions are set to replicate the experimental conditions. The jet inlets are modeled using velocity inlet boundary conditions with a uniform velocity profile at a constant temperature of 302 K and 10% turbulent intensity for both cases. The jet Reynolds number, based on the jet diameter, is used to calculate the velocity value at the inlet. At the outlet, the pressure outlet boundary condition at atmospheric pressure (ie, gauge pressure of 0 kPa) is used. A no-slip wall with constant temperature (332 K) boundary condition is used on the target plate. A no-slip adiabatic wall boundary condition is used on the impingement plate and wall

**TABLE 3** Thermophysical properties of the water-Al<sub>2</sub>O<sub>3</sub> nanofluid for different volumetric concentrations

$\phi$ (%)	$\rho_{\text{nf}}$ , kg/m <sup>3</sup>	$\lambda_{\text{nf}}$ , W/m·K	$\mu_{\text{nf}}$ , Pa·s	$C_{p,\text{nf}}$ , J/kg·K
0	996.24	0.616	0.000821	4179.00
0.2	1002.24	0.675	0.000825	4172.40
0.7	1017.30	0.822	0.000835	4158.90
1.5	1041.30	1.056	0.000851	4129.50
3	1086.40	1.497	0.000882	4080.00



**FIGURE 1** A, Computational domain and boundary conditions for case A and case B. B, The geometric configuration for case A. C, Geometric configuration for case B [Color figure can be viewed at [wileyonlinelibrary.com](http://wileyonlinelibrary.com)]

**TABLE 4** Summary of geometric parameters for case A

D	X/D	Z/D	Y/D	S/D	ext.	n
10 mm	52.5	3	5	5	75 mm	9

**TABLE 5** Summary of geometric parameters for case B

<b>D</b>	<b>X/D</b>	<b>Z/D</b>	<b>Y/D</b>	<b>S/D</b>	<b>ext.</b>	<b>n</b>	<b>p/D</b>	<b>c/D</b>	<b>h/D</b>
10 mm	52.5	3	5	5	75 mm	9	1	1	1

used to produce the crossflow. The symmetry boundary condition is used on the walls perpendicular to the streamwise direction.

## 5 | SOLVER SETUP

In the current study, the numerical simulations are carried out using ANSYS FLUENT software. The recommendations of the study reported in Reference [33] were taken into consideration for setting up the cases. A three-dimensional steady-state case is setup with double precision, employing pressure-based solver neglecting body forces. The Semi-Implicit Method for Pressure-Linked Equations algorithm for pressure velocity coupling is used. The second-order upwind scheme is used to discretize all the governing equations. The low Reynolds number technique is used to model the wall effects. It is done by setting  $y^+$  of the first cell normal to the wall less than one. The residuals limit is set to be  $10^{-6}$  as the convergence criterion for all the governing equations.

The jet Reynolds number and mass flow rate are estimated as follows:

$$Re = \frac{\rho V D_j}{\mu}, \quad (16)$$

$$\dot{m} = \rho V n \frac{\pi}{4} D_j^2, \quad (17)$$

where  $V$  represents the jet inlet velocity,  $D_j$  is the jet diameter, and  $n$  is number of jets.

The projected area-averaged Nusselt number  $Nu_{avg}$ , based on the projected area  $A$  of the target plate, wetted area-averaged Nusselt number  $Nu_{w,avg}$ , based on the wetted area  $A_{w,avg}$ , and the local Nusselt number  $Nu$  are calculated as follows:

$$Nu_{avg} = \frac{\dot{q} D_j}{A(T_w - T_j) \lambda}, \quad (18)$$

$$Nu_{w,avg} = \frac{\dot{q} D_j}{A_{w,avg}(T_w - T_j) \lambda}, \quad (19)$$

**TABLE 6** Summary of grid convergence index study for case A with air as the working fluid at  $Re = 35\,000$ 

<b>Grid</b>	<b>No. of elements (<math>10^6</math>)</b>	<b><math>y^+</math></b>	<b><math>Nu_{w,avg}</math></b>
Coarse	1.45	0.883	98.40
Medium	2.53	0.851	100.11
Fine	4.40	0.801	101.01

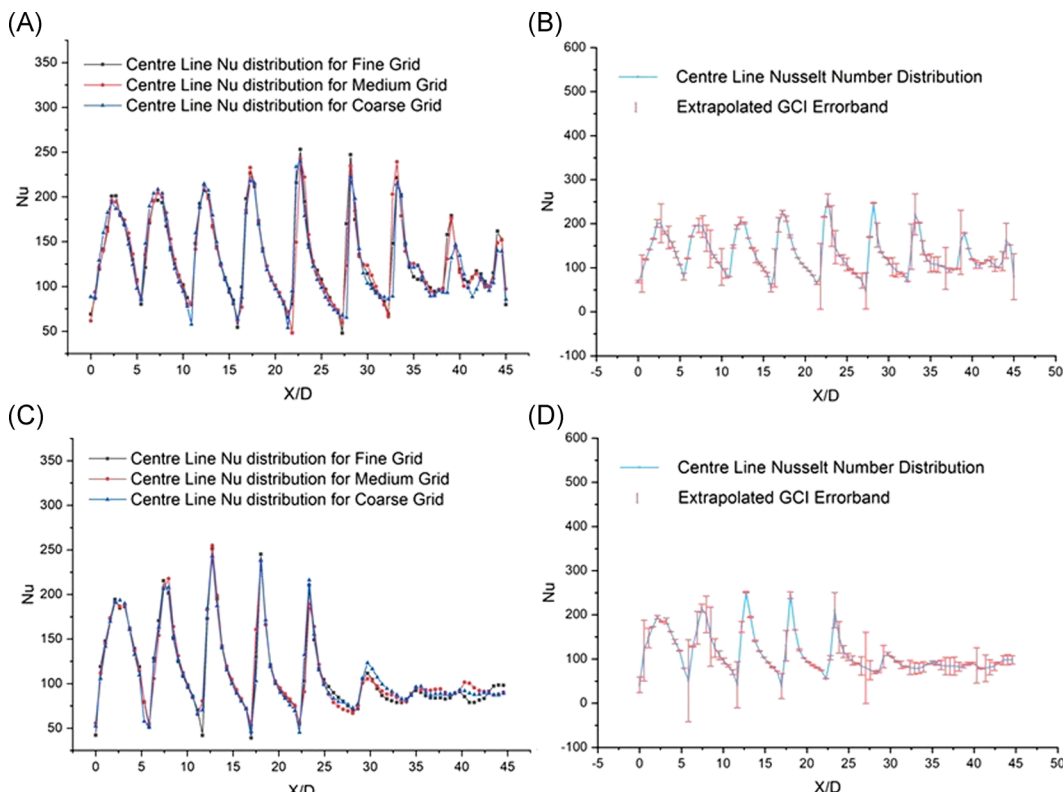


**FIGURE 2** A comparison of the centerline local Nusselt number distributions for different grids of (A) case A and (C) case B, centerline local grid convergence index (GCI) values on the target plate for (B) case A and (D) case B at  $Re = 35\,000$  with air as the working fluid [Color figure can be viewed at [wileyonlinelibrary.com](http://wileyonlinelibrary.com)]

$$Nu = \frac{\dot{q}D_j}{(T_w - T_j)\lambda}, \quad (20)$$

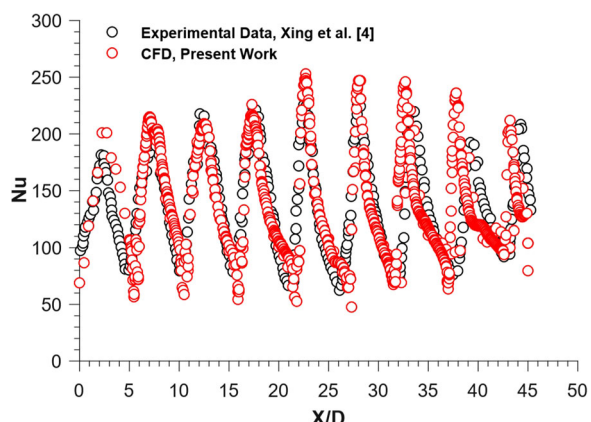
where  $T_w$ ,  $T_j$ ,  $\dot{q}$ ,  $A$ ,  $A_{w,\text{avg}}$ , and  $\lambda$  represent temperature of the target plate, jet's inlet temperature, heat flux over the target plate, projected area of the heated plate, wetted area of the target plate and fins, and thermal conductivity of the working fluid, respectively.

The relation between wetted area and projected area-averaged Nusselt numbers is expressed as follows:

**TABLE 7** Summary of grid convergence index study for case B with air as the working fluid at  $Re = 35\,000$

Grid	No. of elements ( $10^6$ )	$y^+$	$Nu_{w,\text{avg}}$
Coarse	1.55	0.765	80.22
Medium	2.71	0.775	83.09
Fine	4.74	0.797	84.14

**FIGURE 3** A comparison between the experimental and the predicted local Nusselt number distribution of the current study along the centerline for case A with air as the working fluid at  $Re = 35\,000$  [Color figure can be viewed at [wileyonlinelibrary.com](http://wileyonlinelibrary.com)]



$$Nu_{w,\text{avg}} = Nu_{\text{avg}} \frac{A}{A_{w,\text{avg}}} \quad (21)$$

## 6 | GRID INDEPENDENCE STUDY

A grid sensitivity analysis is done to estimate and reduce the discretization errors, which occur due to an inadequate mesh refinement. In the current study, the grid convergence index (GCI) approach proposed in the study reported in Reference [33] is used to obtain grid-independent results. The aforementioned approach is developed on Roache's work.<sup>34</sup>

For case A, three systematically refined unstructured grids with tetrahedral elements, with a constant refinement ratio  $r$  of 1.2, are made to calculate GCI values. For near-wall treatment, inflation layers of prism elements are constructed on the target plate to obtain  $y^+$  of the first cell normal to the wall less than one. The properties of grids used for the GCI study of case B and predicted values of  $Nu_{w,\text{avg}}$  are reported in Table 6. The numerical simulations are carried out with air as a working fluid at Reynolds number 35 000 to compare the numerical predictions with the experimental data. Figure 2A shows a comparison between the centerline local Nusselt number distributions of case A for fine, medium, and coarse grids. The local Nusselt number distributions do not vary, as the mesh refinement is improved. Similarly, Figure 2B shows extrapolated GCI values for centerline local Nusselt numbers for case B. The GCI value for grids of case A is found to be 1.18%, based on wetted area-averaged Nusselt numbers.

The GCI analysis for case B is done in the same way. Three grids with a constant refinement ratio were constructed with tetrahedral elements having an inflation layer of prism elements at the target wall. The properties of the grids used for the GCI study of case B and predicted  $Nu_{w,\text{avg}}$  values are reported in Table 7. The GCI value is found to be 0.89% for wetted area-averaged Nusselt numbers. Figure 2C shows a comparison of the centerline local Nusselt Number distributions for the three grids, whereas Figure 2D shows extrapolated local GCI values for case B.

## 7 | MODEL VALIDATION

The numerical results of case A (flat plate) and case B (pin fin-roughened target plate) are validated with the experimental data. The validation is done to check the accuracy of the

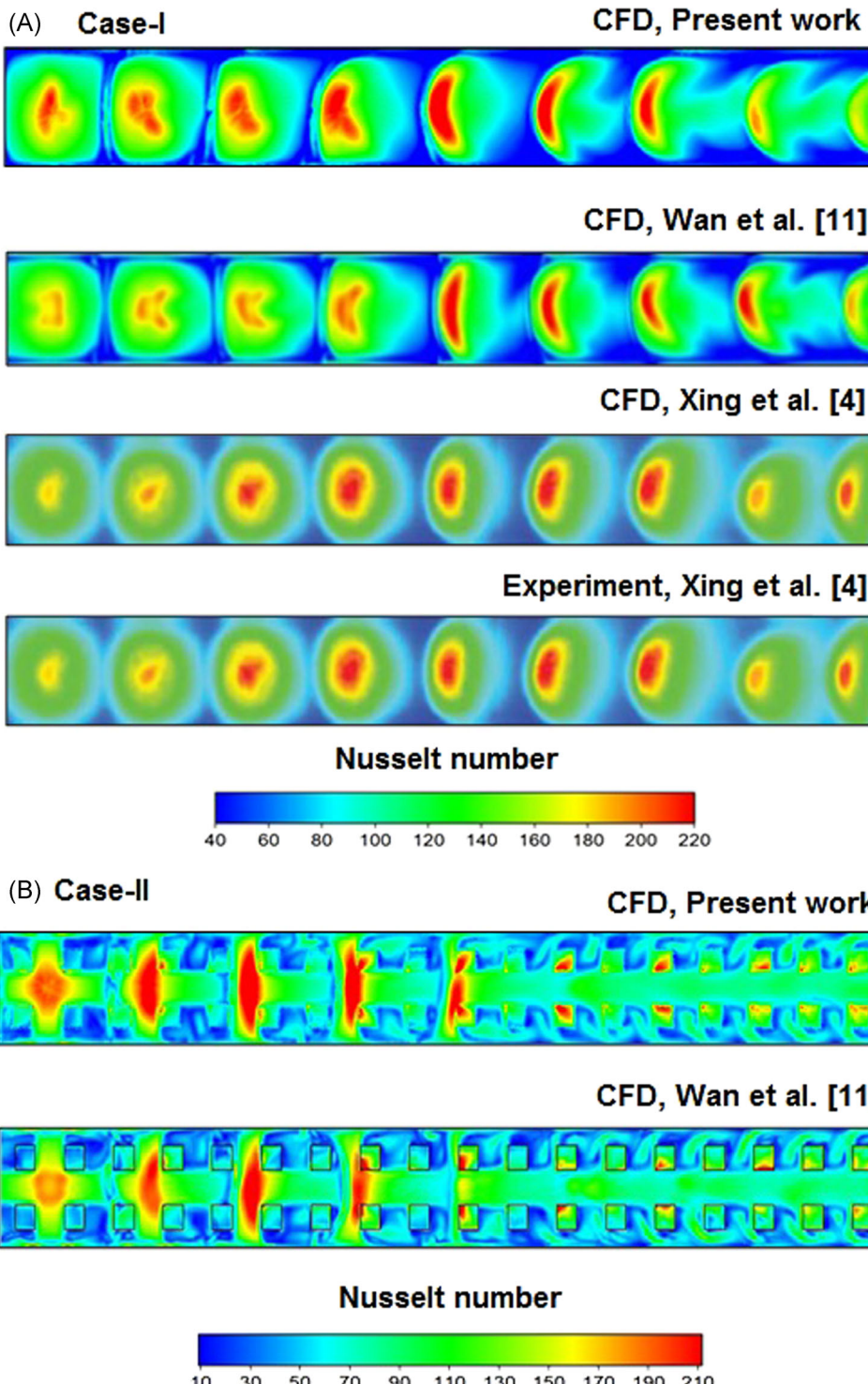
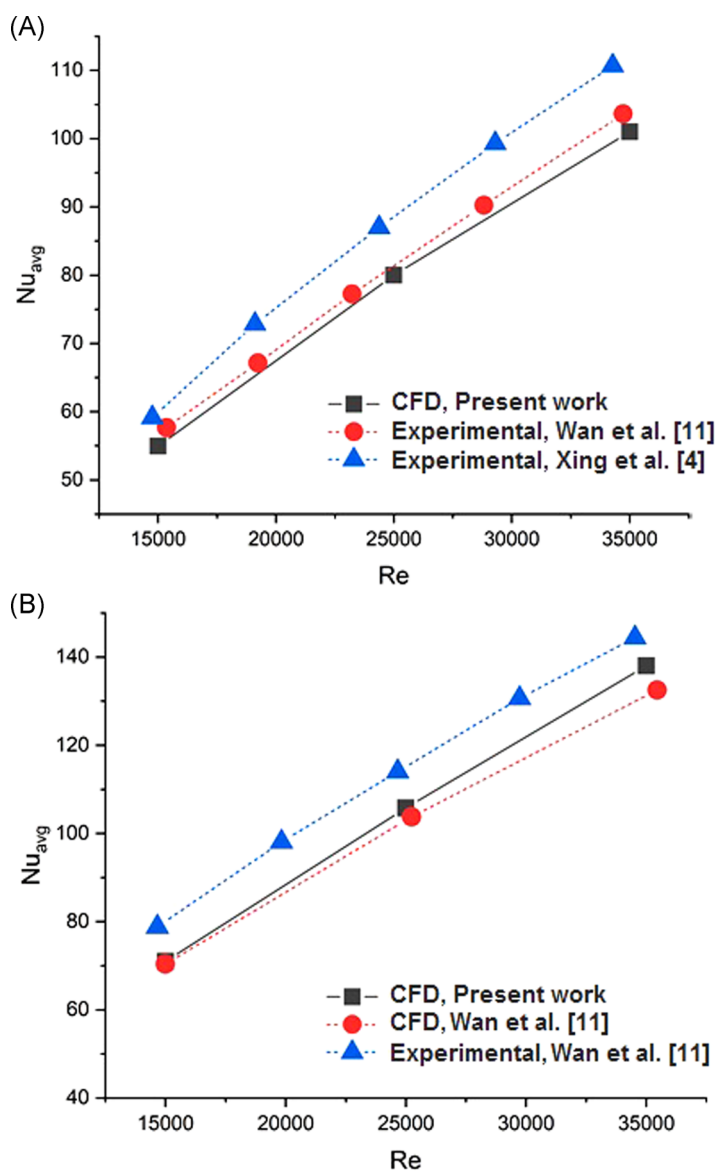


**FIGURE 4** A comparison of the local Nusselt number contours of the current study with the literature results for (A) case A and (B) case B with air as the working fluid at  $Re = 35\,000$  [Color figure can be viewed at [wileyonlinelibrary.com](http://wileyonlinelibrary.com)]

**FIGURE 5** A comparison between the experimental and predicted results of the current study with air as the working fluid for (A) case A and (B) case B [Color figure can be viewed at [wileyonlinelibrary.com](http://wileyonlinelibrary.com)]



numerical model used in the current study. Figure 3 shows a comparison of the computed local Nusselt number values along the centerline with the experimental data of Xing et al.<sup>4</sup> for case A with air as the working fluid at  $Re = 35\,000$ . The predicted local Nusselt number values match very well with the experimental data. Similarly, Figure 4A shows a comparison of the computed local Nusselt number contours on the target wall with the experimentally observed contours of Wan et al.<sup>11</sup> and already published CFD contours of Xing et al.<sup>4</sup> and Wan et al.<sup>11</sup> for case A with air as the working fluid at  $Re = 35\,000$ . The predicted local Nusselt number contours match very well with the experimental and previous numerical results. Figure 5A shows a comparison of the computed projected area-averaged Nusselt number  $Nu_{avg}$  values with the experimental data of Wan et al.<sup>11</sup> and Xing et al.<sup>4</sup> for case A with air as the working fluid. The numerical values of  $Nu_{avg}$  match satisfactorily well with the experimental data. Similarly, the numerical results of case B with air as the working fluid at  $Re = 35\,000$  are compared with the experimental and

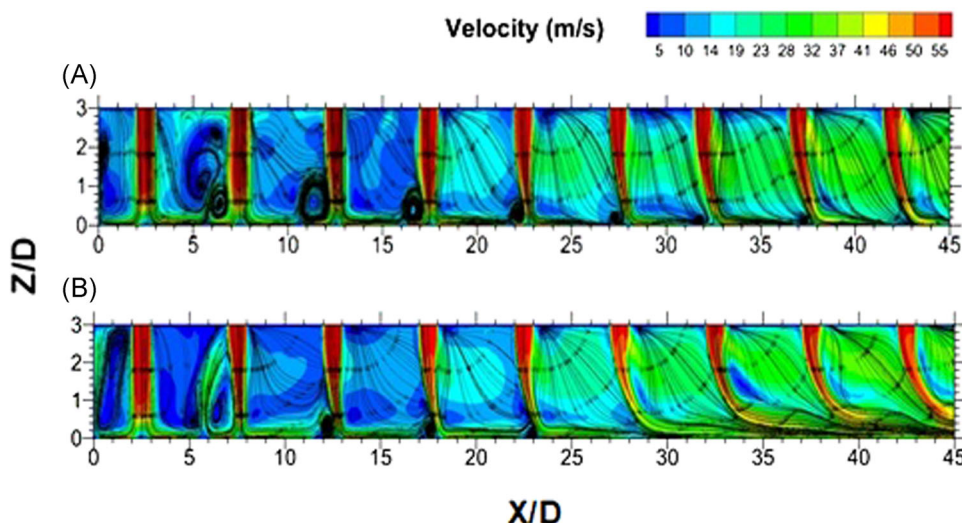


**FIGURE 6** A comparison of velocity contours for (A) case A and (B) case B on the longitudinal central plane with air as the working fluid at  $Re = 35\,000$  [Color figure can be viewed at [wileyonlinelibrary.com](http://wileyonlinelibrary.com)]

numerical results of Wan et al.<sup>11</sup> Figure 4B compares the predicted local Nusselt number contours of the current work with the results of Wan et al<sup>11</sup> for case B with air as the working fluid at  $Re = 35\,000$ . Similarly, Figure 5B shows a comparison of the computed projected area-averaged Nusselt number  $Nu_{avg}$  values with the experimental and numerical data of Wan et al<sup>11</sup> for case B with air as the working fluid. The results match satisfactorily well with the experimental data. Also, the results obtained in the current numerical study are relatively closer to the experimental data when compared with the numerical results obtained by Wan et al,<sup>11</sup> as shown in Figure 5B.

The aforementioned validations of the current numerical predictions with the experimental data confirm the accuracy of the current numerical model. The current model is used to predict the thermal and flow performance of the water-Al<sub>2</sub>O<sub>3</sub> jet impingement cases with and without pin fins.

## 8 | RESULTS AND DISCUSSION

The flow field and thermal characteristics of water-Al<sub>2</sub>O<sub>3</sub> nanofluid jet impingement over the target plate with and without pin fins under a crossflow condition are discussed in this section at different values of  $\phi$ . The comparison begins by first discussing the air-jet impingement case results.

### 8.1 | Flow field

Figures 6A,B present a comparison of velocity contours on the longitudinal central plane for case A and case B, respectively, with air as the working fluid at  $Re = 35\,000$ . An overall

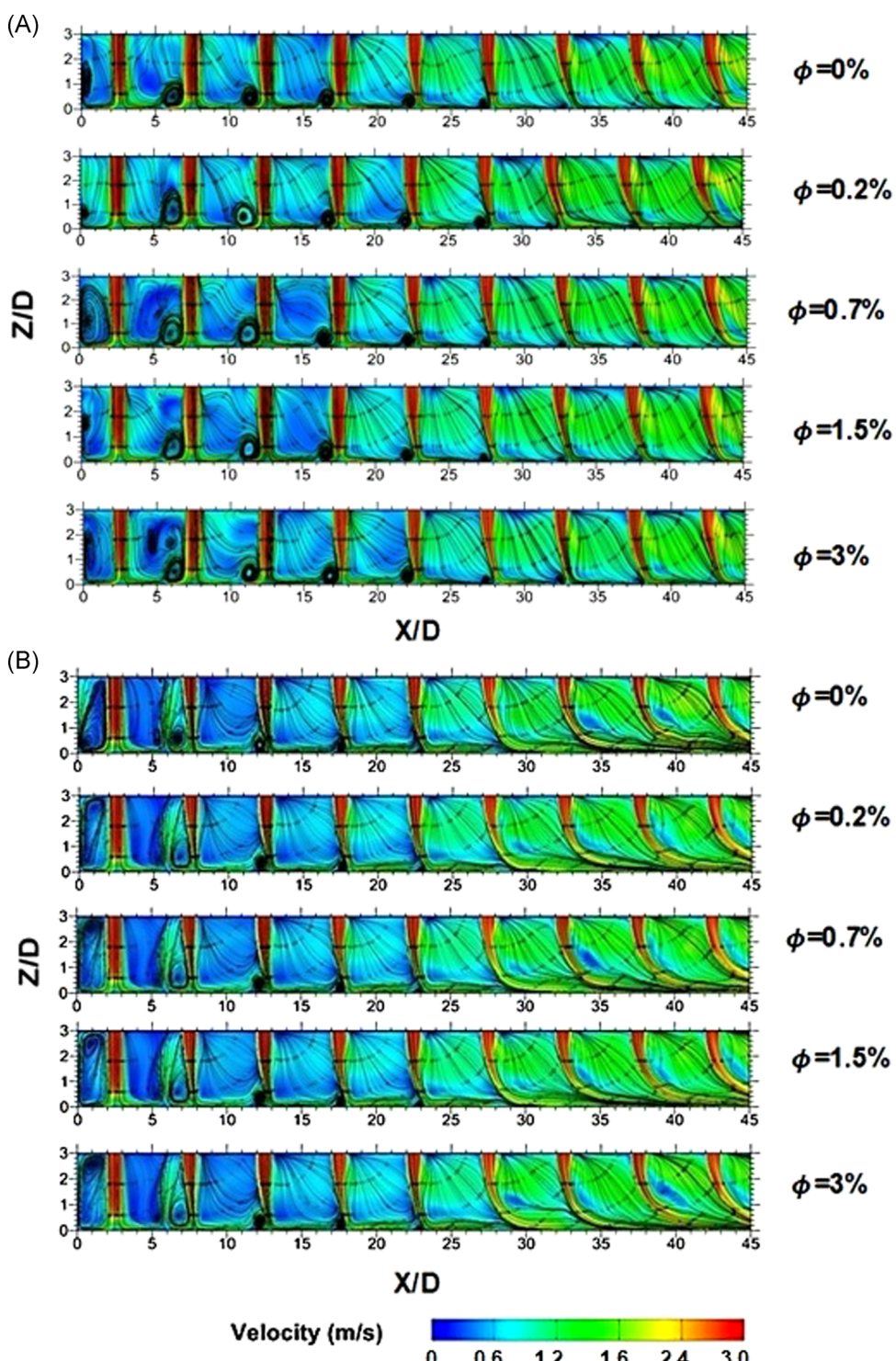


**FIGURE 7** A comparison of velocity contours for (A) case A and (B) case B on the longitudinal central plane for different concentrations of nanoparticles at  $Re = 35000$  [Color figure can be viewed at [wileyonlinelibrary.com](http://wileyonlinelibrary.com)]

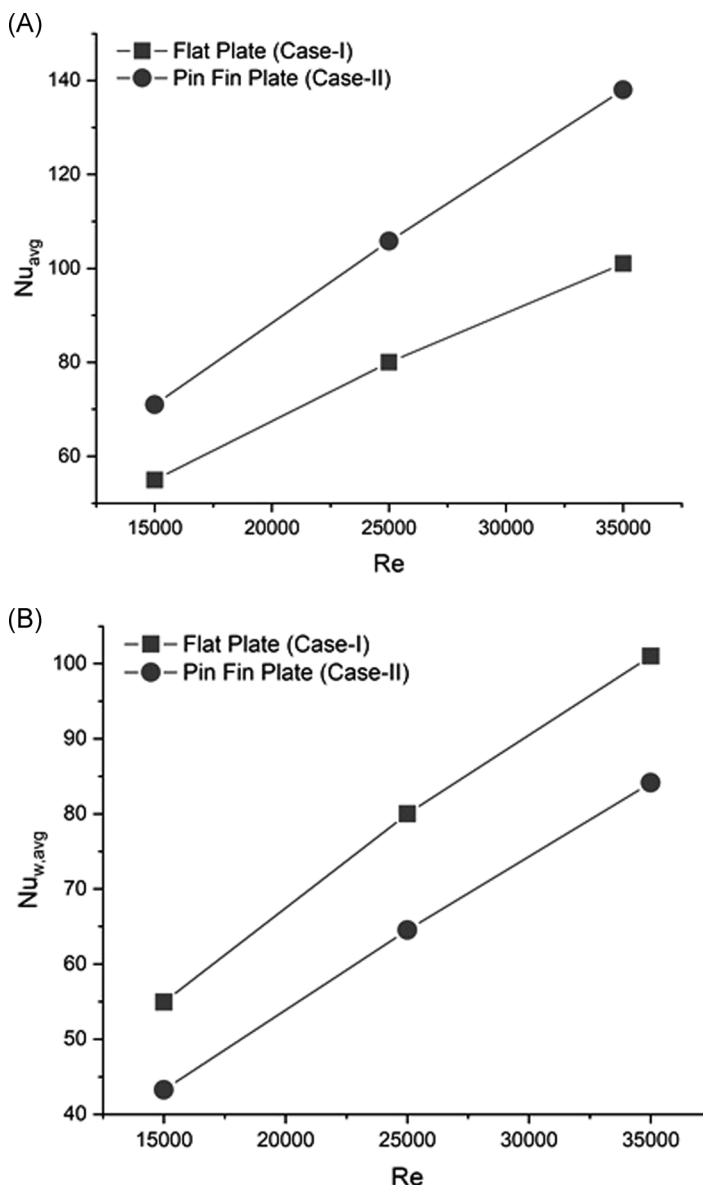


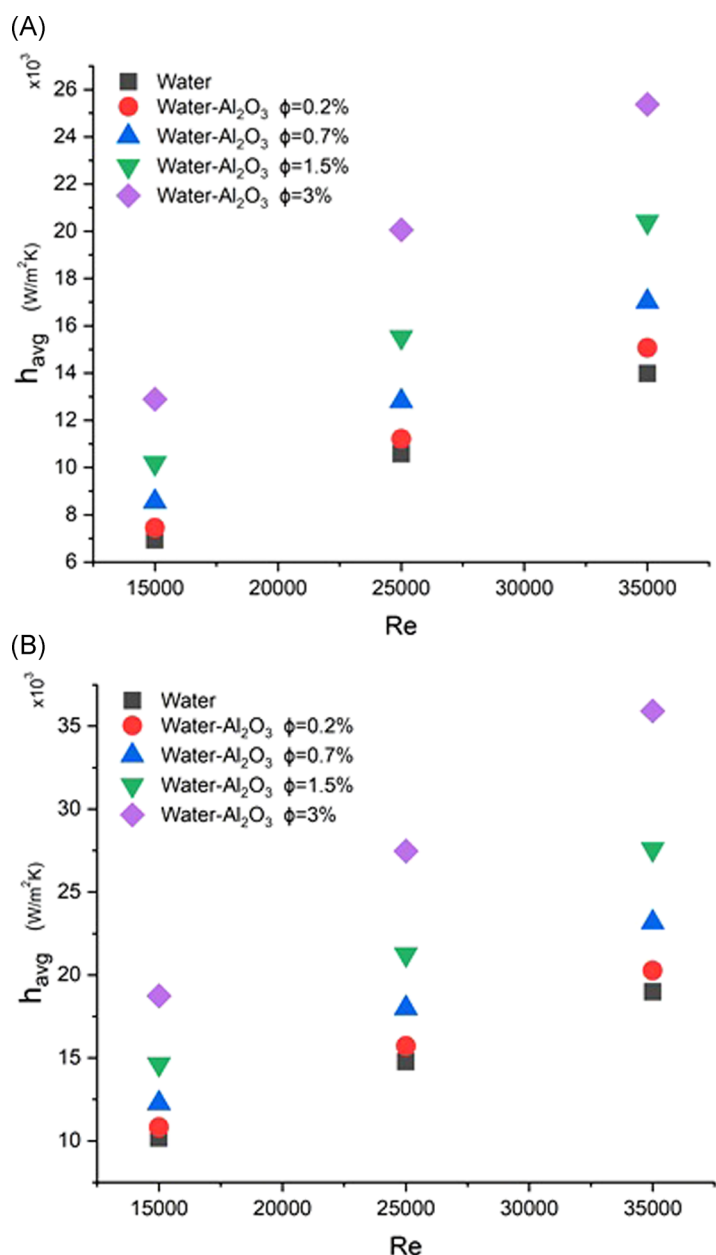
**FIGURE 8** A comparison of (A) the projected area-averaged Nusselt number and (B) the wetted area-averaged Nusselt number values with air as the working fluid for case A and case B

acceleration of fluid in the downstream region of case B can be observed, which hence affects the local thermal performance in the downstream section as compared with case A.

Figure 7A presents velocity contours with streamlines on the longitudinal central planes at different concentrations of nanoparticles ( $\phi = 0\%-3\%$ ) for case A (flat plate) with water as the base fluid at  $Re = 35\,000$ . No change in flow structures and vorticity is observed with the addition of the nanoparticles. However, to keep the jet's Reynolds number constant, the inlet velocity slightly decreases to compensate for an increase in the density of the nanofluid.

The velocity contours with streamlines on the longitudinal central planes at different concentrations of nanoparticles ( $\phi = 0\%-3\%$ ) for case B (pin fin-roughened targeted plate) with water as the base fluid at  $Re = 35\,000$  are shown in Figure 7B. The presence of pin fins results in a higher flow acceleration in the downstream section than observed in the flat plate case.

**FIGURE 9** A comparison of the average convective heat transfer coefficient values for (A) case A and (B) case B for different volumetric concentrations of nanoparticles [Color figure can be viewed at [wileyonlinelibrary.com](http://wileyonlinelibrary.com)]



## 8.2 | Heat transfer

Figure 8A shows a comparison of the projected area-averaged Nusselt number  $Nu_{avg}$  values for case A and case B with air as the working fluid. The roughening of the target plate with pin fins significantly enhances the overall thermal performance as compared with the flat plate. The pin fins, in case B, have 80% more area than the flat plate. Hence, a larger area would result in higher heat flux over the target plate, which means that more heat transfer will occur. This enhancement in heat transfer can be observed through the projected area-averaged Nusselt number obtained using Equation (18), as shown in Figure 8A.

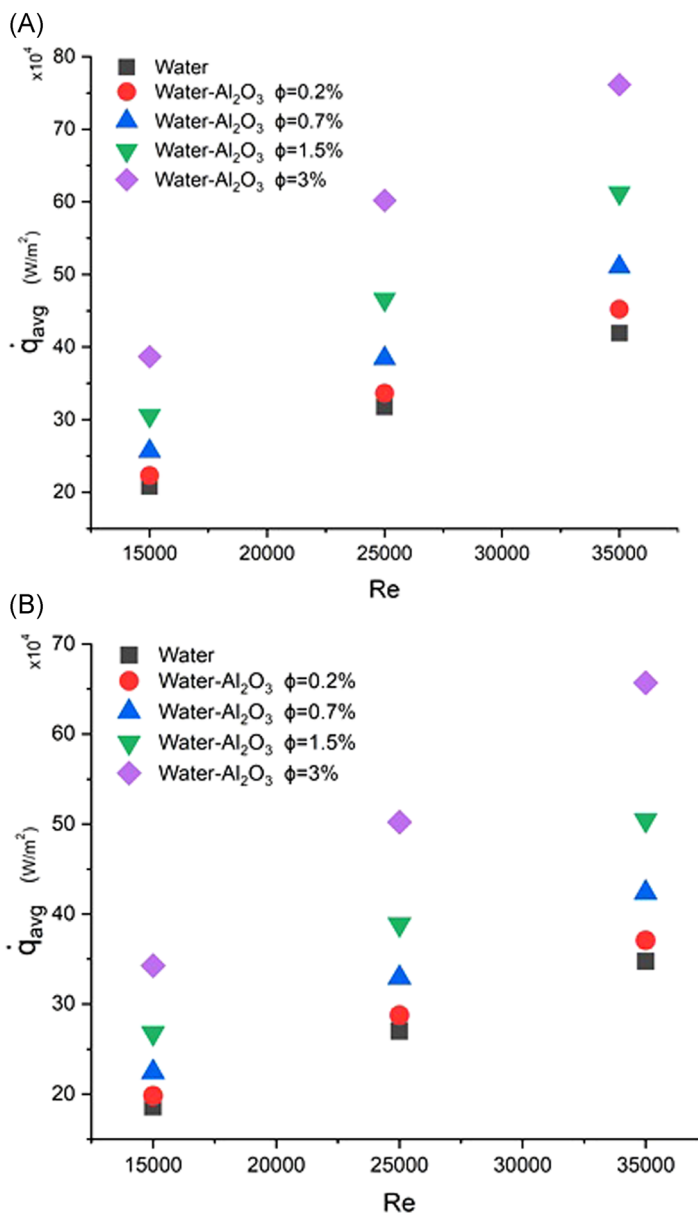


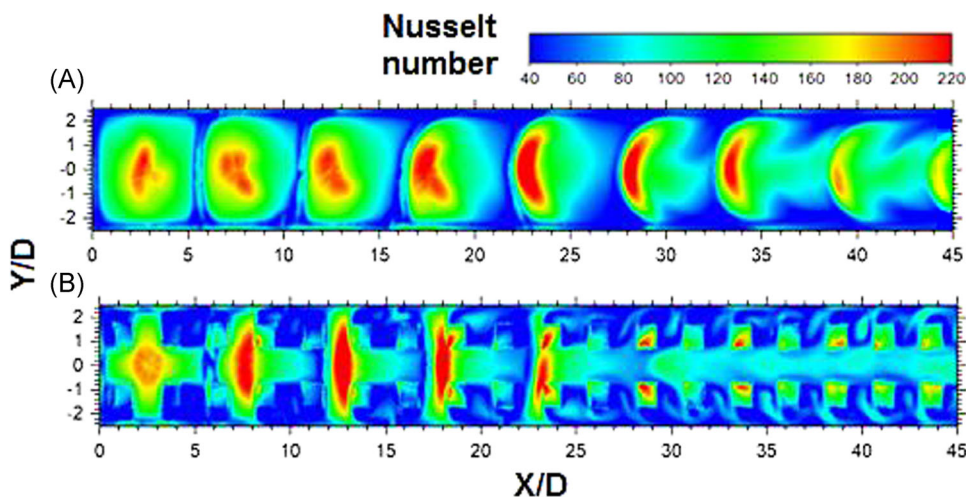
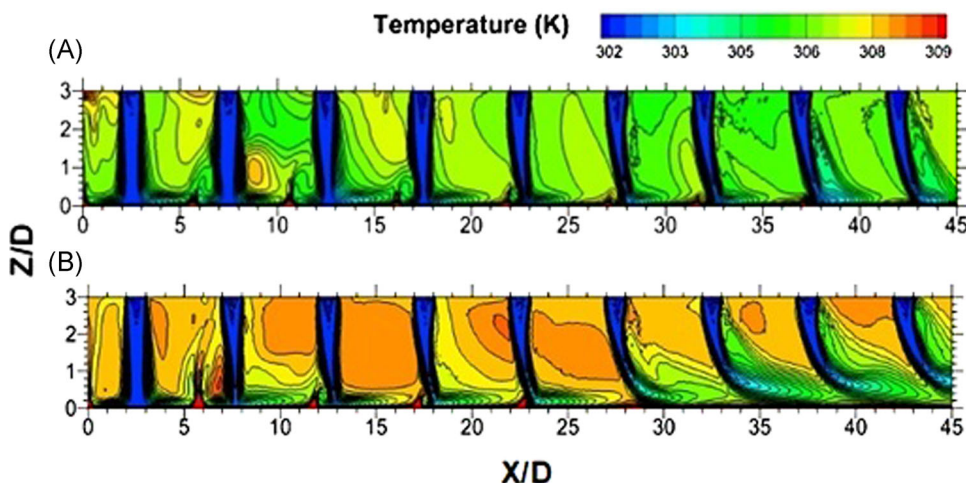
**FIGURE 10** A comparison of the average heat flux values for (A) case A and (B) case B for different volumetric concentrations of nanoparticles [Color figure can be viewed at [wileyonlinelibrary.com](http://wileyonlinelibrary.com)]

**TABLE 8** Comparison of average heat transfer characteristics of case A at  $Re = 35\,000$

$\phi$ (%)	$\frac{q_{nf}}{q_b}$	$\frac{h_{nf}}{h_b}$
0.2	1.078	1.109
0.7	1.217	1.333
1.5	1.460	1.714
3	1.815	2.429

**TABLE 9** Comparison of average heat transfer characteristics of case B at  $Re = 35\,000$ 

$\phi$ (%)	$\frac{\dot{q}_{nf}}{\dot{q}_b}$	$\frac{h_{nf}}{h_b}$
0.2	1.067	1.109
0.7	1.219	1.333
1.5	1.452	1.714
3	1.891	2.430

**FIGURE 11** A comparison of the local Nusselt number contours over the target plate for (A) case A and (B) case B with air as the working fluid at  $Re = 35\,000$  [Color figure can be viewed at [wileyonlinelibrary.com](http://wileyonlinelibrary.com)]**FIGURE 12** A comparison of temperature contours of (A) case A and (B) case B on a longitudinal central plane with air as the working fluid at  $Re = 35\,000$  [Color figure can be viewed at [wileyonlinelibrary.com](http://wileyonlinelibrary.com)]

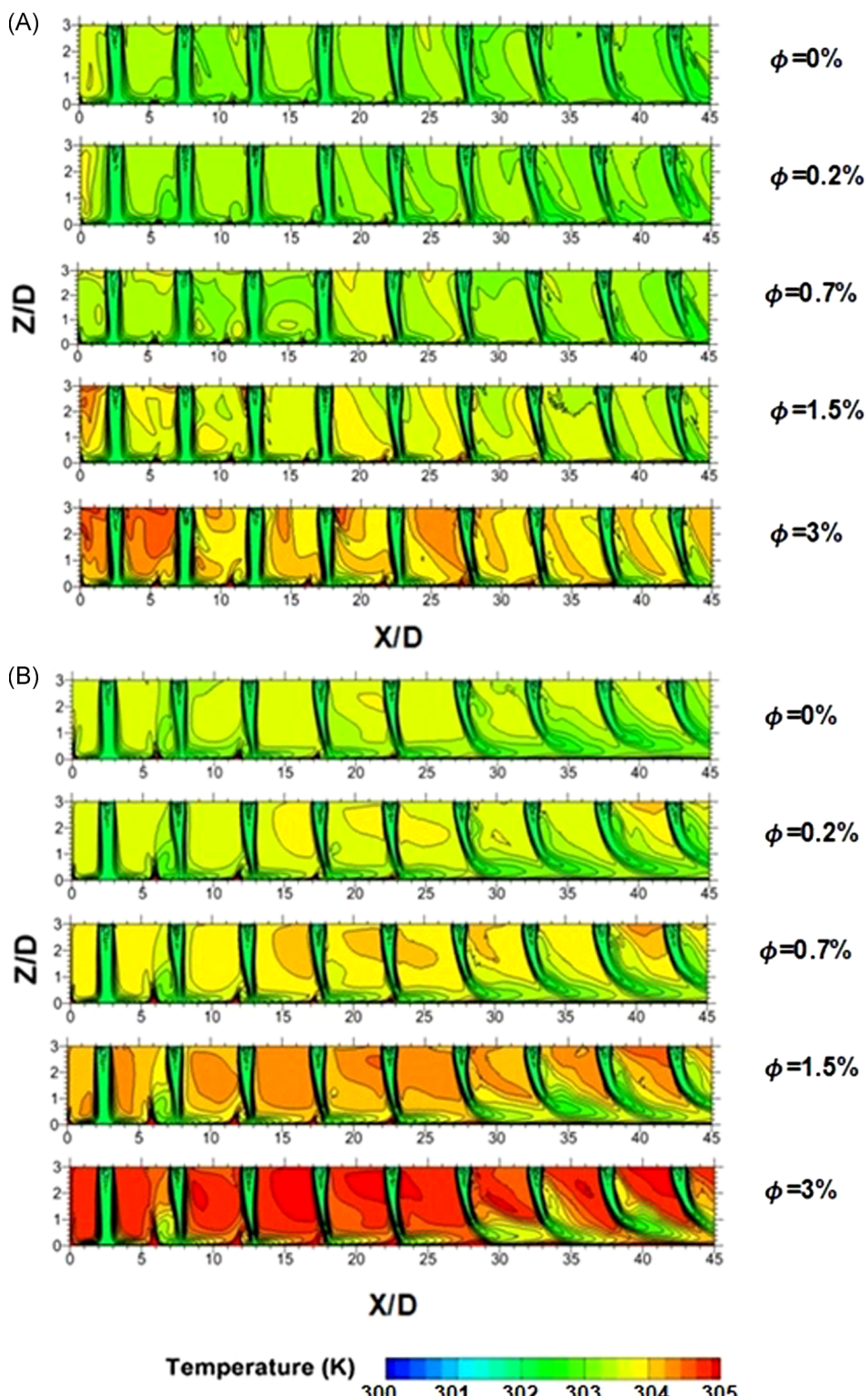


**FIGURE 13** A comparison of temperature contours of (A) case A and (B) case B for different concentrations of nanoparticles on a longitudinal central plane at  $Re = 35\,000$  [Color figure can be viewed at [wileyonlinelibrary.com](http://wileyonlinelibrary.com)]

Figure 8B shows a comparison of the wetted area-averaged Nusselt number  $Nu_{w,\text{avg}}$  values for case A and case B with air impingement.  $Nu_{w,\text{avg}}$  refers to the determination of the average Nusselt number, considering the complete surface area of the target plate and pin fins that come in contact with the working fluid. A decrease in the wetted area-averaged Nusselt number values for case B, compared with case A, also indicates that the primary cause of the heat transfer augmentation is due to a rise in the area rather than the increase in turbulence due to roughening of the target plate by pin fins.

Figure 9A,B show a comparison of average heat transfer coefficient values for case A and case B, respectively, with different concentrations of  $\text{Al}_2\text{O}_3$  nanoparticles in water. Similarly, Figure 10A,B show a comparison of average heat flux values for case A and case B, respectively, with different volumetric concentrations of  $\text{Al}_2\text{O}_3$  nanoparticles. An increase in the heat transfer coefficient and heat flux values with an increase in the  $Re$  and  $\phi$  values can be observed for both cases. It is observed that an increase in  $\phi$  of nanoparticles allows better heat extraction, which is due to the increase in thermal conductivity of the nanofluid. The comparison of heat transfer characteristics of the nanofluid with different  $\phi$  values with the base fluid (water) is shown in Tables 8 and 9. The addition of nanoparticles shows an increment in the heat flux and convective heat transfer coefficient values. The increase in heat transfer coefficient and heat flux over the target plate makes the use of the nanoparticles appealing for applications where high heat extraction is required. Similar trends are also reported in a recent study.<sup>35</sup>

Figure 11A,B show a comparison of the local Nusselt number contours for case A and case B, respectively, with air as the working fluid at  $Re = 35\,000$ . A local cooling performance by impinging jets for both cases can be observed through these contours.

Figure 12A,B show temperature contours on longitudinal central planes for case A and case B, respectively, with air as the working fluid at  $Re = 35\,000$ . The temperature inside the jet regions remains relatively low and almost the same as that of the inlet temperature for both cases. The effect of area enhancement can be seen for case B as compared with case A, as it results in a higher domain temperature. The effect of crossflow can also be seen, as the downstream temperature is comparatively lower for all the cases. Figure 13A,B show the effect of  $\phi$  on temperature contours for case A and case B, respectively, with water as the base fluid at  $Re = 35\,000$ . The effective thermal conductivity of the nanofluid and temperature in the domain are increased by the addition of nanoparticles. The temperature inside the jet regions and also in the downstream region remains low for all concentrations of nanoparticles.

## 9 | CONCLUSIONS

An array of multiple impinging jets with air, water, and water- $\text{Al}_2\text{O}_3$  nanofluid in a maximum crossflow configuration over the target plate with and without pin fins is numerically investigated. Simulations are carried out at a fixed jet-to-target plate distance ( $Z/D = 3$ ), different volumetric concentrations of  $\text{Al}_2\text{O}_3$  ( $\phi = 0.2\%, 0.7\%, 1.5\%$ , and  $3\%$ ), and different jet Reynolds numbers ( $Re = 15\,000, 25\,000$ , and  $35\,000$ ). The numerical results are validated with the experimental data. The following results can be concluded from the study:

- No effect on flow features is observed with the addition of nanoparticles.
- An increase in the convective heat transfer coefficient and heat flux over the target plate is observed with the increase in the volumetric concentration of  $\text{Al}_2\text{O}_3$ . About 81.5% and 89.1%

augmentation in the average heat flux values is observed for flat and pin fin-roughened target plates, respectively, for  $\phi = 3\%$ .

- An increase in temperature is observed with an increase in the volumetric concentration, which is aided by the increased thermal conductivity of the working fluid.

In the future, a similar setup can be used to investigate the effects of different nanoparticles, other than  $\text{Al}_2\text{O}_3$ , and different surface enlargement elements, other than pin fins, on the thermal and fluid flow performance of impinging jet systems. The different jet inlet conditions that modulate the jet turbulence and shear layer development, for example, pulsating or synthetic jets, different nozzle shapes, nozzle characteristics length, and so on, can also be explored as a future research work.

## DATA AVAILABILITY STATEMENT

Data available on request from the authors.

## NOMENCLATURE

$A$	area of target plate
$D$	jet diameter
ext.	extended surface of domain
$F_s$	factor of safety for grids
GCI	grid convergence index
$h$	convection heat transfer coefficient
$k$	turbulent kinetic energy
$n$	number of jets
$Nu$	Nusselt number
$Pr$	Prandtl number
$\dot{q}$	heat flux
$Re$	jet Reynolds number
$r$	refinement ratio
$V$	jet inlet velocity
$y$	normal coordinate
$y^+$	first cell distance normal to wall

## GREEK SYMBOLS

$\phi$	volumetric concentration
$\rho$	density
$\lambda$	thermal conductivity
$\mu$	absolute viscosity
$\vartheta$	kinematic viscosity
$\omega$	specific dissipation rate

## SUBSCRIPTS

avg	projected area-averaged
b	base fluid
j	inlet jet
n	nanoparticle
nf	nanofluid

t turbulent  
w target plate  
w,avg wetted area-averaged

## DIMENSIONLESS GEOMETRIC RATIOS

$c/D$  dimensionless width of pin  
 $h/D$  dimensionless height of pin  
 $p/D$  dimensionless pitch between pins  
 $S/D$  dimensionless spacing between jets  
 $X/D$  dimensionless streamwise distance  
 $Y/D$  dimensionless spanwise distance  
 $Z/D$  dimensionless jet-to-plate distance

## ACKNOWLEDGMENTS

The Higher Education Commission (HEC), Pakistan, is acknowledged for the financial assistance under SRGP project 2067. Usman Allauddin also acknowledges the contribution of Mr. M. Saad Saeed and Mr. Haseeb Ahsan of NED University of Engineering and Technology.

## ORCID

Usman Allauddin  <http://orcid.org/0000-0003-2351-5018>

## REFERENCES

1. Zuckerman N, Lior N. Jet impingement heat transfer: physics, correlations, and numerical modeling. *Adv Heat Transf.* 2006;39:565-631.
2. Martin H. Heat and mass transfer between impinging gas jets and solid surfaces. *Adv Heat Transf.* 1977;13:1-60.
3. Weigand B, Spring S. Multiple jet impingement—a review. *Heat Transf Res.* 2011;42(2):101-142.
4. Xing Y, Spring S, Weigand B. Experimental and numerical investigation of heat transfer characteristics of inline and staggered arrays of impinging jets. *J Heat Transf.* 2010;132(9):092201.
5. Wae-Hayee M, Tekasakul P, Nuntadusit C. Influence of nozzle arrangement on flow and heat transfer characteristics of arrays of circular impinging jets. *Songklanakarin J Sci Technol.* 2013;35(2):203-212.
6. Caliskan S, Baskaya S, Calisir T. Experimental and numerical investigation of geometry effects on multiple impinging air jets. *Int J Heat Mass Transf.* 2014;75:685-703.
7. Spring S, Xing Y, Weigand B. An experimental and numerical study of heat transfer from arrays of impinging jets with surface ribs. *J Heat Transf.* 2012;134(8):082201.
8. Xing Y, Spring S, Weigand B. Experimental and numerical investigation of impingement heat transfer on a flat and micro-rib roughened plate with different crossflow schemes. *Int J Therm Sci.* 2011;50(7):1293-1307.
9. Rao Y, Chen P, Wan C. Experimental and numerical investigation of impingement heat transfer on the surface with micro W-shaped ribs. *Int J Heat Mass Transf.* 2016;93:683-694.
10. Chen L, Brakmann R, Weigand B, Rodriguez J, Crawford M, Poser R. Experimental and numerical heat transfer investigation of an impingement jet array with V-ribs on the target plate and on the impingement plate. *Int J Heat Fluid Flow.* 2017;68:126-138.
11. Wan C, Rao Y, Chen P. Numerical predictions of jet impingement heat transfer on square pin-fin roughened plates. *Appl Therm Eng.* 2015;80:301-309.
12. Zeitoun O, Ali M. Nanofluid impingement jet heat transfer. *Nanoscale Res Lett.* 2012;7:139.
13. Modak M, Srinivasan S, Garg K, Chougule SS, Agarwal MK, Sahu SK. Experimental investigation of heat transfer characteristics of the hot surface using  $\text{Al}_2\text{O}_3$ -water nanofluids. *Chem Eng Process.* 2015;91:104-113.
14. Modak M, Chougule SS, Sahu SK. An experimental investigation on heat transfer characteristics of hot surface by using CuO-water nanofluids in circular jet impingement cooling. *J Heat Transf.* 2017;140(1):012401.
15. Naphon P, Nakharintr L, Wiriyasart S. Continuous nanofluids jet impingement heat transfer and flow in a micro-channel heat sink. *Int J Heat Mass Transf.* 2018;126:924-932.

16. Barewar SD, Tawri S, Chougule SS. Heat transfer characteristics of free nanofluid impinging jet on flat surface with different jet to plate distance: An experimental investigation. *Chem Eng Process*. 2019;136:1-10.
17. Londhe KD, Deshpande SU, Sidheshwar RK. Effect of nanofluid jet impingement on its heat transfer enhancement and pumping power. *Int Eng Res J*. 2016;1-6.
18. Nguyen CT, Galanis N, Polidori G, Fohanno S, Popa CV, Le Bechec A. An experimental study of a confined and submerged impinging jet heat transfer using  $\text{Al}_2\text{O}_3$ -water nanofluid. *Int J Therm Sci*. 2009;48(2):401-411.
19. Allauddin U, Mahrukh M, Rehman NU, Haque ME, Uddin N. Numerical investigation of heat transfer by an impinging jet using alumina-water nanofluid. *Numer Heat Transf A*. 2018;74(8):1486-1502.
20. Lorenzo GD, Manca O, Nardini S, Ricci D. Numerical study of laminar confined impinging slot jets with nanofluids. *Adv Mech Eng*. 2012;4:248795.
21. Manca O, Mesolella P, Nardini S, Ricci D. Numerical study of a confined slot impinging jet with nanofluids. *Nanoscale Res Lett*. 2011;6:188.
22. Senkal C, Torii S. Thermal fluid flow transport phenomena in nanofluid jet array impingement. *J. Flow Visual Image Process*. 2015;22(1-3):59-79.
23. Darwish AM, El-Kersh AMR, El-Sheikh MN, El-Moghazy IM. A review on nanofluid impingement jet heat transfer. *Int J Nanotechnol Allied Sci*. 2017;1:1-15.
24. Menter FR. Two-equation eddy-viscosity turbulence models for engineering applications. *AIAA J*. 1994; 32(8):1598-1605.
25. Brakmann R, Chen L, Weigand B, Crawford M, Experimental and numerical heat transfer investigation of an impinging jet array on a target plate roughened by cubic micro pin-fins. *Proceedings of Turbo Expo: Power for Land, Sea and Air*. Montreal, Quebec, Canada, 2015.
26. Zu YQ, Yan YY, Maltson JD, CFD prediction for multi-jet impingement heat transfer. *Proceedings of Turbo Expo: Power for Land, Sea and Air*. Orlando, FL, 2010.
27. Peng W, Jizu L, Minli B, Yuyan W, Chengzhi H. A numerical investigation of impinging jet cooling with nanofluids. *Nanoscale Microscale Thermophys Eng*. 2014;18(4):329-353.
28. Sahoo BC, Vajjha RS, Ganguli R, Chukwu GA, Das DK. Determination of rheological behavior of aluminum oxide nanofluid and development of new viscosity correlations. *Pet Sci Technol*. 2009;27(15):1757-1770.
29. Saini D, Agarwal GD. Thermophysical properties of nanofluids—a review. *Int J Adv Eng Sci Technol*. 2016; 5(1):39-45.
30. Bhattacharya P, Saha SK, Yadav A, Phelan PE. Brownian dynamics simulation to determine the effective thermal conductivity of nanofluids. *J Appl Phys*. 2004;95(11):6492-6494.
31. Brinkman HC. The viscosity of concentrated suspensions and solutions. *J Chem Phys*. 1952;20(4):571.
32. Pak BC, Cho YI. Hydrodynamic and heat transfer study of dispersed fluids with submicron metallic oxide particles. *Exp Heat Transf*. 1998;11(2):151-170.
33. Celik IB, Ghia U, Roache PJ. Procedure for estimation and reporting of uncertainty due to discretization in CFD applications. *J Fluids Eng*. 2008;130(7):078001.
34. Roache PJ. Quantification of uncertainty in computational fluid dynamics. *Annu Rev Fluid Mech*. 1997;29:123-160.
35. Allauddin U, Jamil T, Shakaib M, et al. Heat transfer enhancement caused by impinging jets of  $\text{Al}_2\text{O}_3$ -water nanofluid on a micro-pin fin roughened surface under crossflow conditions—a numerical study. *J Enhanc Heat Transf*. 2020;27(4):367-387.

**How to cite this article:** Allauddin U, Mohiuddin R, Khan HMU, Uddin N, Khan WA. Nanoscale heat transfer investigation of an array of impinging jet systems with different working fluids under crossflow with and without pin fins. *Heat Transfer*. 2020;1-24.  
<https://doi.org/10.1002/htj.21986>